Radio-Frequency Energy Harvesting Using Rapid 3D Plastronics Protoyping Approach: A Case Study

Xuan Viet Linh Nguyen, Tony Gerges, Pascal Bevilacqua, Jean-Marc Duchamp, Philippe Benech, Jacques Verdier, Philippe Lombard, Pangsui Usifu Linge, Fabien Mieyeville, Michel Cabrera, et al.

Journal of
Low Power Electronics and Applications

MDPI

Article

Radio-Frequency Energy Harvesting Using Rapid 3D Plastronics Protoyping Approach: A Case Study

Xuan Viet Linh Nguyen [1], Tony Gerges [1], Pascal Bevilacqua [1], Jean-Marc Duchamp [2], Philippe Benech [2], Jacques Verdier [1], Philippe Lombard [1], Pangsui Usifu Linge [1], Fabien Mieyeville [1], Michel Cabrera [1] and Bruno Allard [1,*]

[1] Univ Lyon, INSA Lyon, Université Lyon1, Ecole Centrale de Lyon, CNRS, Ampère, UMR5005, 69100 Villeurbanne, France
[2] Univ Grenoble-Alpes, CNRS, Grenoble INP, G2Elab, UMR5269, 621 Av. Centrale, 38400 Saint-Martin-d'Hères, France
* Correspondence: bruno.allard@insa-lyon.fr; Tel.: +33-472438238

Abstract: Harvesting of ambient radio-frequency energy is largely covered in the literature. The RF energy harvester is considered most of the time as a standalone board. There is an interest to add the RF harvesting function on an already-designed object. Polymer objects are considered here, manufactured through an additive process and the paper focuses on the rapid prototyping of the harvester using a plastronic approach. An array of four antennas is considered for circular polarization with high self-isolation. The RF circuit is obtained using an electroless copper metallization of the surface of a 3D substrate fabricated using stereolithography printing. The RF properties of the polymer resin are not optimal; thus, the interest of this work is to investigate the potential capabilities of such an implementation, particularly in terms of freedom of 3D design and ease of fabrication. The electromagnetic properties of the substrate are characterized over a band of 0.5–2.5 GHz applying the two-transmission-line method. A circular polarization antenna is experimented as a rapid prototyping vehicle and yields a gain of 1.26 dB. A lab-scale prototype of the rectifier and power management unit are experimented with discrete components. The cold start-up circuit accepts a minimum voltage of 180 mV. The main DC/DC converter operates under 1.4 V but is able to compensate losses for an input DC voltage as low as 100 mV (10 µW). The rectifier alone is capable of 3.5% efficiency at −30 dBm input RF power. The global system of circularly polarized antenna, rectifier, and voltage conversion features a global experimental efficiency of 14.7% at an input power of −13.5 dBm. The possible application of such results is discussed.

Keywords: energy harvesting; 3D Plastronics; radio frequency; array of antenna; stereolithography; electroless deposition

Citation: Nguyen, X.V.L.; Gerges, T.; Bevilacqua, P.; Duchamp, J.-M.; Benech, P.; Verdier, J.; Lombard, P.; Linge, P.U.; Mieyeville, F.; Cabrera, M.; et al. Radio-Frequency Energy Harvesting Using Rapid 3D Plastronics Protoyping Approach: A Case Study. *J. Low Power Electron. Appl.* **2023**, *13*, 19. https://doi.org/10.3390/jlpea13010019

Academic Editors: Alessandro Bertacchini and Pierre Gasnier

Received: 15 December 2022
Revised: 25 January 2023
Accepted: 13 February 2023
Published: 17 February 2023

1. Introduction

The dissemination of Internet-of-Things (IoTs)-like wireless sensors or other tiny computing machines is facing a serious issue regarding the power supply. Batteries are no longer a suitable choice, or at least the effective lifespan must be enlarged as much as possible. Harvesting energy in the IoT environment is investigated. Among the possible sources of ambient energy, the electromagnetic field yields a weaker potential but is still significant. An electromagnetic field harvester comprises four blocks to convert radio-frequency (RF) energy to direct-current (DC) energy, namely an antenna, a matching network, a rectifier and a voltage converter. Shape of antenna, topology of matching network, rectifier or voltage converter, or combination of functions have been studied to create simple to complex systems.

A review of radio-frequency energy harvester (RFEH) design is given in [1]. Most RFEHs have been considered for a frequency range below 5 GHz, though microwave

applications have been reported recently [2]. The major metrics of performances are the minimum input RF power that can start-up the EH system, the open-voltage at the targeted input RF power level and the effective efficiency when the rectenna is loaded with an impedance equal to its internal impedance (optimal load condition) [3].

Figure 1 pictures a landscape of representative results of the rectenna from the literature, where the maximum efficiency is mentioned along with the related input RF power level [4,5]. The results are related to demonstrators obtained through a traditional 2D process. The results are discriminated depending on the rectifier topology and the selected diode. Colors and symbols identify the various results in Figure 1. At low input RF power (<−20 dBm), one-diode topology (symbols $\oplus$ and $\otimes$ in Figure 1) is mostly preferred among the well-known topologies (single series, single shunt, voltage doubler, Dickson topology, Cockcroft-Walton topology, Diode bridge topology, Villard charge pump topology, etc). The two-diode topology is proposed at medium input RF power (0 dBm) for implementing voltage doubling effect. The maximum efficiency is in direct relation with the input RF power: more input voltage enables to better bias the diodes (or even MOSFET transistors in the case of integrated circuit implementations). Complex rectifier topologies are considered for input RF power levels well above 0 dBm. The selection of diode is spread among the different results. However, the references HSMS2850 and SMS7621 dominate at low input RF power.

Ambient RF energy harvesting is related to a case of low RF power. In this condition, the expected DC voltage at the rectenna output is quite low and supplying a (low-power) circuit requires at least 1 V as an order of magnitude with respect to CMOS electronics. Multi-level topologies have been experimented, but due to diode forward voltage drop, a quite high level of input RF power is necessary [6].

Most papers consider 50 Ω rectenna for ease of design and characterization. It was already demonstrated that a different value of characteristic impedance would be beneficial in the case of very low ambient RF energy [7]. The situation is more complex with respect to design and test and it is not considered here.

The matching network between the antenna and the rectifier relies on micro-strip implementation as it reduces the bill-of-material. Demonstrators in the literature are fabricated on substrates for which dielectric performances (losses) are quite optimal, i.e., close to Rogers' substrates ones. Some exploratory studies are carried out on FR4 for the sake of cost, but it is not a game-changer yet. Other substrates such as paper [8] have also been experimented and the losses of the dielectric impact the rectenna performances in quite the same way as the one reported in this paper.

Antenna geometries benefit from constant improvement with original shapes in 2D or 3D. The literature covers few proposals of antenna or rectennas [5,9] obtained from a combination of additive manufacturing to create the device substrate and through metallization to obtain the conductive traces. Otherwise, adding an RFEH capability to an existing IoT object is not simple if it should be obtained seamlessly [1]. Besides, IoT objects may offer a package with a sufficient external surface for implementing an antenna and receiving additional devices related to the RFEH. It is an issue of selective metallization. This idea is already investigated with wearable IoTs [10]. In this context, the prototypes are fabricated using additive manufacturing, namely 3D printing and deposition of conductive inks. The conductivity of ink is pointed to as a limitation.

The literature covers few proposals of antennas obtained from additive manufacturing. Moreover, additive manufacturing [11] is preferred for the manufacturing of low-count series of IoTs or when prototyping an IoT object. Additive manufacturing is in use regarding cellphone antennas or 5G-related antennas [12,13]. In the same perspective, the paper focuses on the capability of adding an RFEH capability to an existing object package or housing using 3D plastronic prototyping of the objects. Indeed, the polymer material involved in the additive manufacturing as well as the added conductor have a major impact on the RFEH performances and it is one of the main issues of the paper to quantify the impact and discuss the pertinence of the manufacturing process proposal in this context.

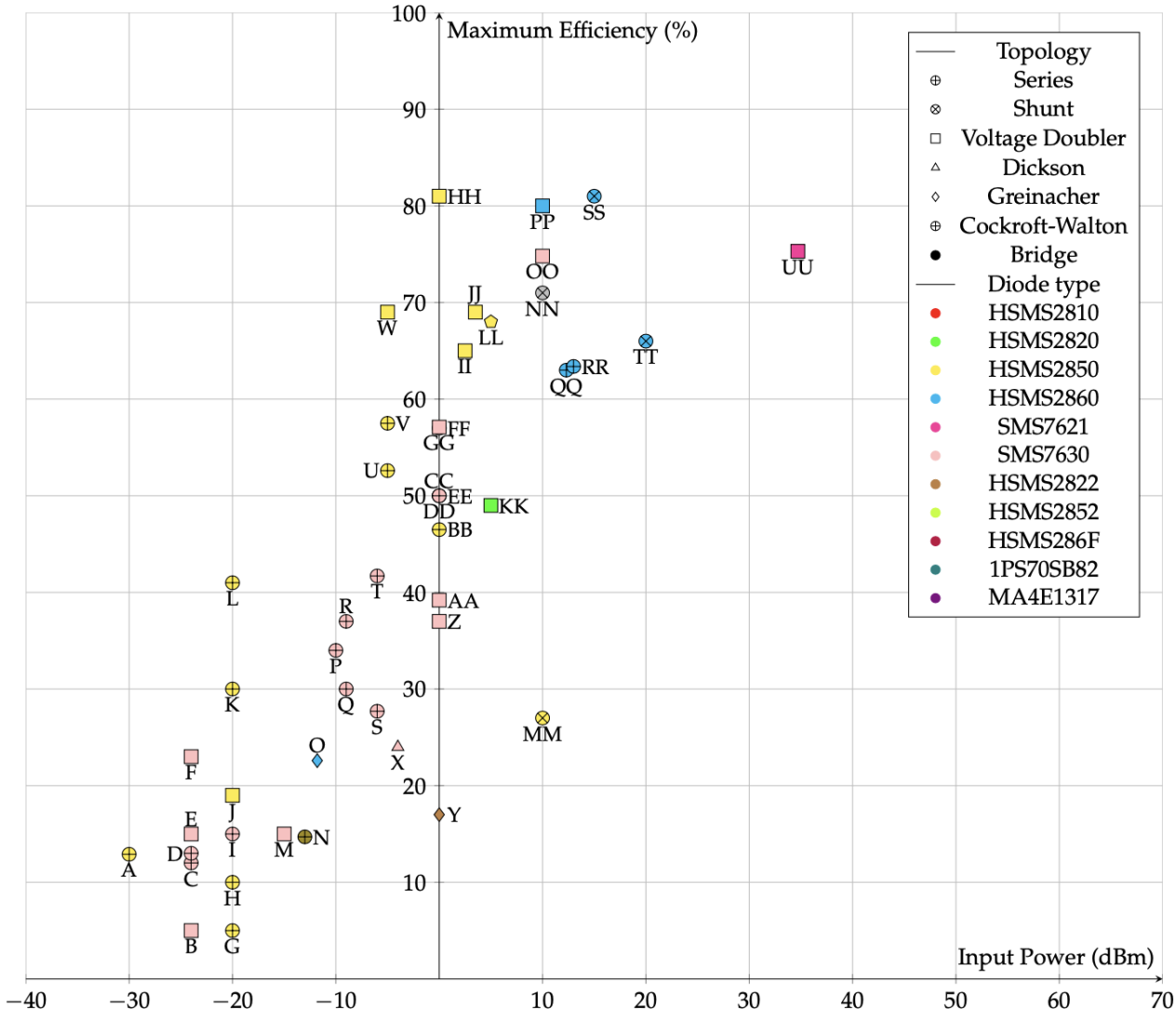

Figure 1. Recent State of the art on rectifier: Maximum Efficiency vs Input Power depending on topology and diode reference. A-[14], B-[15], C-[16], D-[17], E-[15], F-[15], G-[8], H-[8], I-[18], J-[19], K-[20], L-[21], M-[22], N-[4], O-[23], P-[24], Q-[25], R-[25], S-[26], T-[26], U-[27], V-[27], W-[28], X-[29], Y-[30], Z-[31], AA-[32], BB-[33], CC-[33], DD-[34], EE-[9], FF-[35], GG-[32], HH-[36], II-[28], JJ-[37], KK-[5], LL-[19], MM-[38], NN-[39], OO-[31], PP-[40], QQ-[41], RR-[42], SS-[43], TT-[44], UU-[45].

3D Plastronics allows integrating electronic functions at the surface of the polymer housing of an object by selective metallization of conductive traces and placement of Surface Mount Devices (SMD) [46,47]. 3D Plastronics is the terminology now accepted by the IPC organization [48], but it is also known as Molded Interconnect Devices or Mechatronic Integrated Devices (MID) [47]. It plays an important role in different application domains, such as miniaturization of electronic devices [49], thermal management [50], medical equipment's [46], automotive [51] or telecommunications [52]. Rapid 3D Plastronics is a new method in the field of additive manufacturing. The strategy is based on the manufacturing of the polymer support by 3D printing (often Stereolithography) and selective metallization by electroless copper (Cu).

This paper details the design and measurement of an RFEH vehicle fabricated on a substrate using a 3D stereolithography printing method (SLA) associated to electroless copper deposition (EDL) as a rapid prototyping process. SLA resin is not recyclable yet, including the one considered in the case study but on the one hand printing is inexpensive and straightforward, and on the other hand treatment toward recyclability is progressing.

This paper discusses gradually the main aspects of a rectenna (antenna, rectifier, voltage conversion), given a material and a manufacturing process that are not supposed to be suitable for RF applications. The sections cover the aspects sequentially with results for a partial conclusion. The paper content is organized as follows. Section 2 details the two-transmission-line method introduced to evaluate the electromagnetic properties of the printed substrate. A simple patch antenna supports a comparison between Rogers substrate and the printed one to confirm the applicability to RF applications. Section 3 details a modified patch antenna and the array of four-antenna. Section 4 covers the series, one diode rectifier with a particular focus on the internal impedance of the rectifier as it is a major parameter for the power management unit. Section 5 summarizes the design of the power management circuit deduced from the literature. Section 6 details important system-level measurements and comparison to the state of the art. The principal knowledge deduced from the case study is discussed prior to the conclusion.

2. Printed Substrate Characterization

Prior to designing printed RF circuits, key parameters must be identified: the relative permittivity (ϵ_r) and the loss tangent (tanδ) of the substrate. An easily printable resin is selected throughout the work: the high-temperature (HT) resin, grades V1 and V2 from Formlabs [53]. The latter SLA resins are optimized for the 3D stereolithography printing method using Formlabs; dedicated printers and a satisfying surface roughness is obtained [11]. The resins are selected also for good thermal properties regarding brazing surface-mount-devices (SMD) on top of the printed object.

2.1. Dielectric Permittivity and Loss Tangent

Many methods have been developed for characterizing dielectric materials and the two-transmission-line (TTL) method is selected here thanks to its simplicity of implementation over a wide range of frequency (from 1 MHz to 100 GHz) [54]. A 1.5 mm thick sheet is printed in 2D form and then metallized with a 7 µm layer of electroless deposited copper (EDL) (measured by X-ray fluorescence) yielding a 2.2 µΩ.cm resistivity (4-point probe). Lines are laid out using the electroless metallization method with an effective length of 44.5 mm and 79.6 mm, respectively, and an effective width of 3.8 mm. A commercial Rogers 4003C substrate with laminated copper is characterized first for the purpose of calibration with adequate lines. The results are presented in Table 1.

Table 1. Dielectric parameters of common antennas' substrates and HT resins.

Material	Relative Permittivity	Loss Tangent
LCP Vectra E820i	4.3 at 2.45 GHz	0.004 at 2.45 GHz
PolyEtherEtherKeton (PEEK)	3.2	0.002
Pocan DP T 7140 LDS	4.1	0.0138
Pocan TP 710-003 LDS	3.26	0.01
PPS with 40% of fiber glass	4	0.025
Rogers 4003C	3.54 ± 0.02 [0.5–2.5 GHz]	0.003 ± 0.001 [0.5–2.5 GHz]
Formlabs HT Resin v1	3 ± 0.1 [0.5–2.5 GHz]	0.025 ± 0.0025 [0.5–2.5 GHz]
Formlabs HT Resin v2	2.9 ± 0.1 [0.5–2.5 GHz]	0.04 ± 0.0025 [0.5–2.5 GHz]
Future Rogers resin [55]	-	0.01 [0.5–10 GHz]

According to Table 1, the Rogers 4003C dielectric has a higher relative permittivity as well as a lower loss tangent. The SLA resins allow easy 3D printing of complex objects but they are obviously less optimal for RF applications because of dielectric losses. The implication is evaluated on the performance of a simple antenna.

2.2. Simple Patch Antenna

A patch antenna is selected for the sake of simplicity and low-sensitivity to small variations in geometry. Considering the measured ϵ_r and tanδ, the antenna is optimized

at the resonant frequency of 2.45 GHz using CST Studio Suite 2019 (Figure 2) [56]. Two antennas are fabricated, one on a 2D Rogers 4003C substrate and the other on SLA resin printed substrate. The radiating parameters of these antennas are shown in Table 2. Note that the dimensions of the Rogers substrate are identical to the ones of HT Resin V1 printed substrate and the patch manufactured on the Rogers substrate is slightly smaller, thanks to the higher relative permittivity.

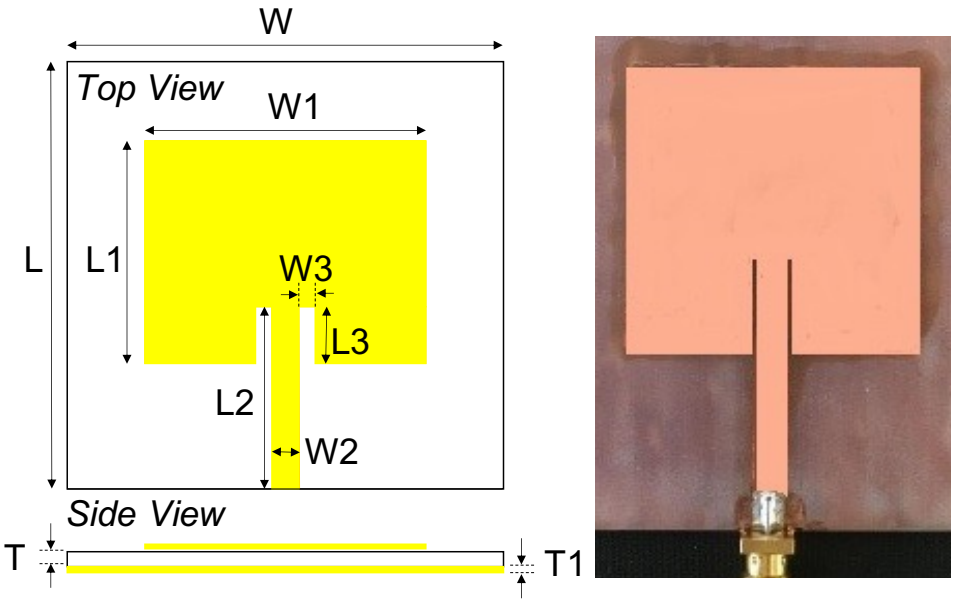

Figure 2. Simple patch antenna manufactured on HT resin V1 printed substrate and electroless copper deposition. Geometrical parameter values in Table 3.

Table 2. Radiation parameters of patch antennas.

Material	Rogers 4003C (Simulation)	Rogers 4003C (Measurement)	HT V1 (Simulation)	HT V1 (Measurement)
frequency range [GHz]	2.438–2.464	2.436–2.459	2.42–2.486	2.41–2.495
Bandwidth [MHz]	26	23	66	85
Resonant freq [GHz]	2.45	2.449	2.453	2.452
Gain [dB]	5.5	5.3	2.4	2.5

Table 3. Geometrical parameter values (in mm) related to the simple antenna in Figure 2.

W	W1	W2	W3	L	L1	L2	L3	T	T1
60	36.1	4	0.7	70	35.15	33	11.05	1.5	0.007

Obviously, the identified dielectric parameters enable a correct design of the printed antenna. The HT resin V1 is not as optimal as the Rogers' dielectric. The bandwidth is wider and, more importantly, the antenna gain is smaller. This means that a given area of the patch antenna will offer access to a lower quantity of power when built from SLA resin, but it is still significant enough to supply a low power sensor or a tiny computing system. This issue is largely discussed in [57]. Particularly, an analytical method is proposed to define a possible antenna geometry depending on the available area at hand.

3. Modified Patch Antenna and Array of Four Antennas

A circularly polarized antenna is considered to capture the electromagnetic field around the IoT object. The package of the IoT object at hand will define the available surface. In the ideal case of a regular 3D package outside surface, such an antenna may be synthesized as an array of four antennas, regularly disposed around the object package. Arrays of multiple but small antennas have been covered but the limit in manufacturing accuracy should be considered first. This issue is clearly discussed in [58]. The design methodology takes care of the antenna design, the isolation factor between antennas but does not consider the complexity of manufacturing. Moreover, Table IV in [58] indicates that the combined DC power from the antennas in the array tends to decrease when the number of antennas is larger than 4.

The square patch is selected for ease of design. However, the complexity of the antenna design is not a limitation in terms of manufacturing here. Thus, all the geometries considered in [58] could be fabricated without specific issues. A similar cylindrical arrangement of square patches is fabricated on a flexible RO5880 substrate with thickness of 0.72 mm and relative permittivity of 2.2 in [59].

The same Schottky diode (SMS7630) will be selected later on in Section 4, and the rectenna load is chosen to be 5.1 kΩ, close to the junction resistance of the diode [60]. A measurement detailed in Section 4 shows that a different choice of resistor value should be considered.

3.1. Modified Patch Antenna for Circular Polarization

Elementary square patch antennas are designed for fabrication using the HT Resin v2 (at one point, the resin v1 was replaced by the grade v2 by the supplier). The length of the antenna is 36 mm for a resonant frequency of 2.45 GHz. A 50 Ω micro-strip transmission line is placed on one side of the antenna, but not necessarily centered for feeding the antenna. The length of this feeding line is shortened to attenuate its effect on the radiation pattern of the antenna (consequently, the gain of the antenna).

The corners are truncated from a height, t (Figure 3a). The feeding line is decentered of a distance, m. The gain and the axial ratio of the patch antenna are optimized through simulation to evaluate the dimension t. The reflection coefficient is affected by the feeding line position. A trade-off is defined, yielding the corner dimension, t (4.7 mm) and decentering parameter, m (+2 mm). The dimensions of the antenna in Figure 3 are listed in Table 4. The simulated axial ratio is 0.7 dB at 2.45 GHz. In addition, the simulated and measured realized gain of the antenna is 2.03 dB and 1.70 dB, respectively.

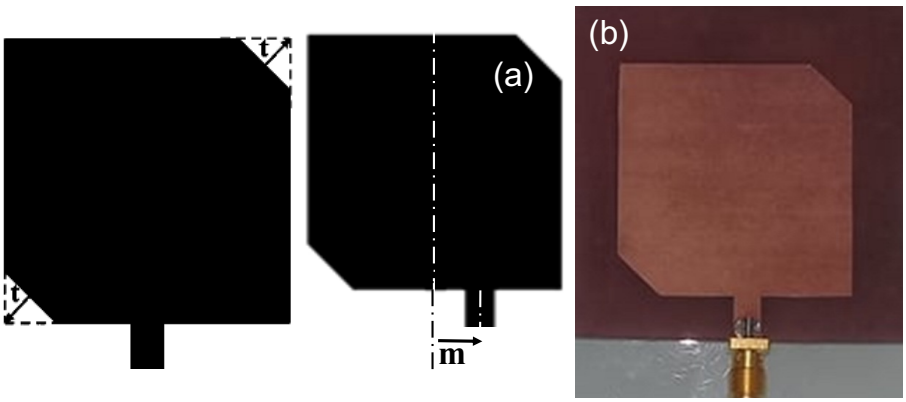

Figure 3. Elementary patch manufactured in HT resin V1. (**a**) design geometry. (**b**) manufactured sample.

Table 4. Geometrical parameter values (in mm) related to the modified antenna in Figure 3.

W	W1	W2	L	L1	L2	t	m
60	36	4	70	36	7	4.7	2

The simulated and measured reflection coefficient of the antenna in Figure 3b is pictured in Figure 4. The reflection coefficient is limited to −17.4 dB. It is nonetheless a satisfying value for considering an array of antennas.

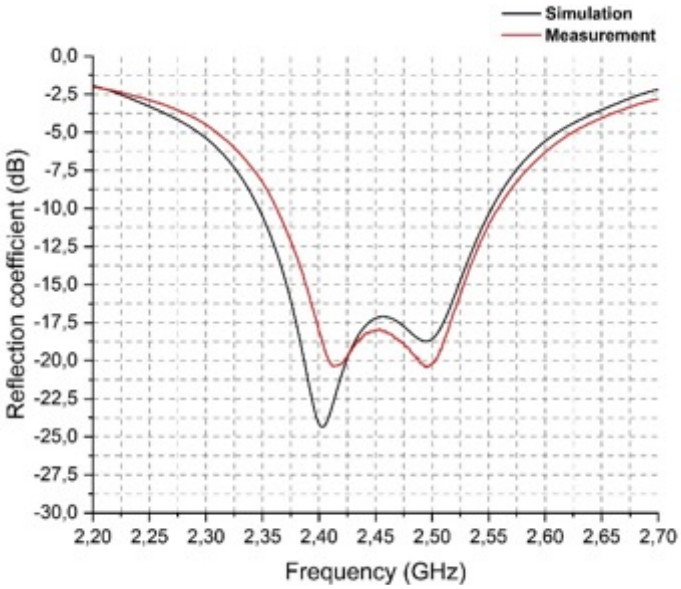

Figure 4. Simulation and experimental reflection coefficient of the antenna in Figure 3b.

The Half-Power Beam Width (HPBW) of the antenna is mentioned in Table 5. For the previous 2D design of elementary patch antennas, the measured HPBW is around 85° in the vertical plane and 80° in the horizontal plane along the the feeding line of the antenna. The idea is then to curve the antennas with a radius in the order of λ to broaden the HPBW in both planes [61,62]. However, the back-lobe of the radiation pattern is smaller with a larger curving radius. The author in [63] studied the impacts of the curving radius on the performance of the circular polarization nearly-square patch antenna at 2.3 GHz. When the curving radius is approximately higher than 3λ, the curvature does not affect the axial ratio of the patch antenna. The flexibility of manufacturing (advantage of rapid prototyping) easily gives access to any geometry, such as a four, curved elementary patch antenna array, as discussed below.

Table 5. Half-power beam width at 2.45 GHz of the planar patch antenna (Figure 3) and the curved antenna (Figure 5).

	Planar Patch	**Curved Patch**
Vertical plane (sim.)	87.1°	92°
Vertical plane (meas.)	85°	90°
Horizontal plane (sim.)	87.9°	94.8°
Horizontal plane (meas.)	80°	83°
Gain (sim.)	2.03 dBic	1.26 dBic
Gain (meas.)	1.7 dBic	1 dBic

3.2. Four-Sector Antenna

A simple four-sector antenna is fabricated as a cylinder Figure 5a with four circularly-shaped patches. The isolation between each elementary patch antenna has been simulated and measured. In Figure 5a, the ground plane is segmented and a plane unique ground plane has also been considered. The latter option impacts negatively the isolation with −38 dB compared to −45 dB with the former option. The radiating parameters of the antennas in both considered options of the ground plane are listed in Table 6. The matching network and the rectifier topology are then designed for the proposed antenna vehicle.

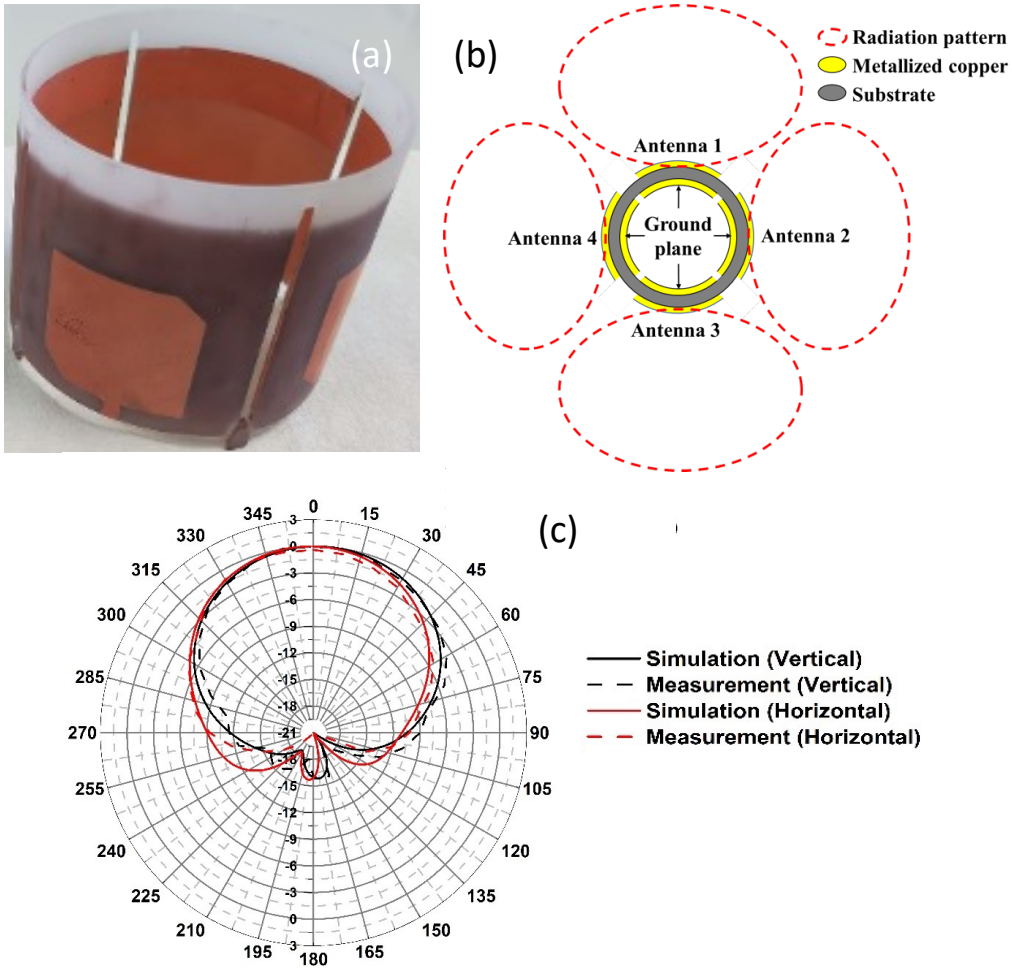

Figure 5. Four curved elementary patch antenna array. (**a**) manufactured sample in HT resin V2. (**b**) Expected radiation pattern. (**c**) Radiation pattern in vertical and horizontal planes of each elementary antenna in the array.

Table 6. Half-power beam width at 2.45 GHz of the curved antenna (Figure 5), depending on the ground plane option.

	Common Ground Option	Segmented Ground Option
Vertical plane (sim.)	92°	94°
Vertical plane (meas.)	90°	90°
Horizontal plane (sim.)	94.8°	88°
Horizontal plane (meas.)	83°	87°
Gain (sim.)	1.26 dBic	1.6 dBic
Gain (meas.)	1 dBic	1.35 dBic

4. Rectifier and Rectenna Internal Impedance

This paper focuses on the harvesting of ambient electromagnetic energy that is very low by essence. A one-diode, series topology is selected. As mentioned in [1] and detailed also in [59], the diode SMS7630-079LF is a good candidate. It is worth noticing that the diode SMS7630-079LF is not as accurately modeled as the diode HSMS2850 in Keysight ADS software. The latter diode is then preferred for design purpose, but the two offered very close performances (threshold voltage, losses, reverse-bias capability).

The matching network uses micro-strip components as they are compatible with the metalization of the printed substrate and a minimal number of SMDs are then brazed on top of the conductive lines. Figure 6b pictures a sample rectifier. The printed substrate is influencing the RF part (matching network) but not the DC-electrical part. The S_{11}

parameter of the rectifier is minimal (−28 dB) for an RF excitation of −24 dBm. The conversion efficiency is pictured in Figure 6c for low input RF power levels. At −30 dBm input power, the conversion efficiency is 3.5% under 5 kΩ optimal load. This means that 350 nW are available to supply a payload, but under a voltage of 12 mV, it requires a voltage conversion to match the need of a standard CMOS circuit. This necessary circuit is detailed in Section 5.

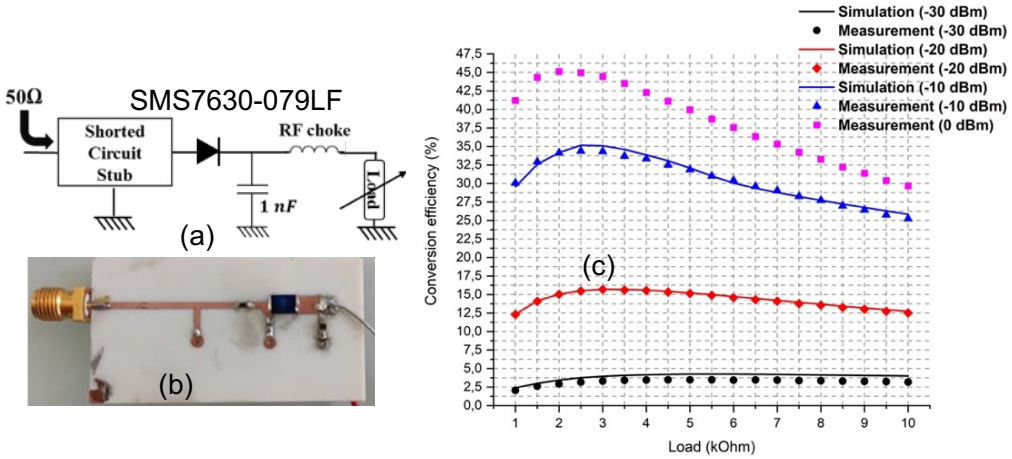

Figure 6. One-diode, series rectifier. (**a**) Electrical circuit. (**b**) Experimental vehicle. (**c**) Conversion efficiency with respect to load.

The measurements in Figure 6c are based on a method to insure a specific input RF power level at the rectifier input, independently of the matching network adequacy with respect to the operating conditions. The setup in Figure 7 is used for the measurements and comprises directional couplers, connectors and cables, where power losses, P_{loss}, must be identified prior to the application to the rectifier. The reflected power, P_r at the rectifier input is measured to deduce the power absorbed by the rectifier input, P_t. The RF generator power level, P_i, is adjusted to set P_r to a given and known level (namely, 0, −10, −20 and −30 dBm, respectively, in Figure 6c). The rectifier output voltage is measured in open-circuit conditions, which implies a certain RF generator power level to obtain the targeted rectifier input RF power. The tuning is repeated for each value of the load at the output of the rectifier. The determination of the rectifier near optimal load benefits from this measurement approach, when the output voltage reaches half the open-circuit voltage value for a same input RF power level.

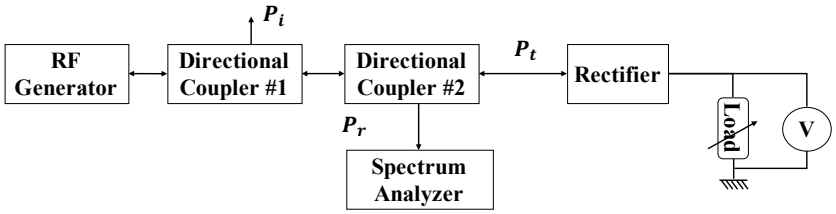

Figure 7. Schematic of the setup regarding the RF supply of the rectifier.

The concept of a circularly polarized patch antenna developed in the previous Section should increase the capturing of the ambient electromagnetic field and boost the conversion efficiency. One option is related to the ground plane, which can be unique or segmented by sector. The segmented ground option is preferred for the purpose of the isolation of the antennas. So, four complementary rectifiers are naturally adopted with a unique DC output (Figure 8). It may be noted that 3D plastronic prototyping enables to fabricate exact similar portions of the rectenna circuit.

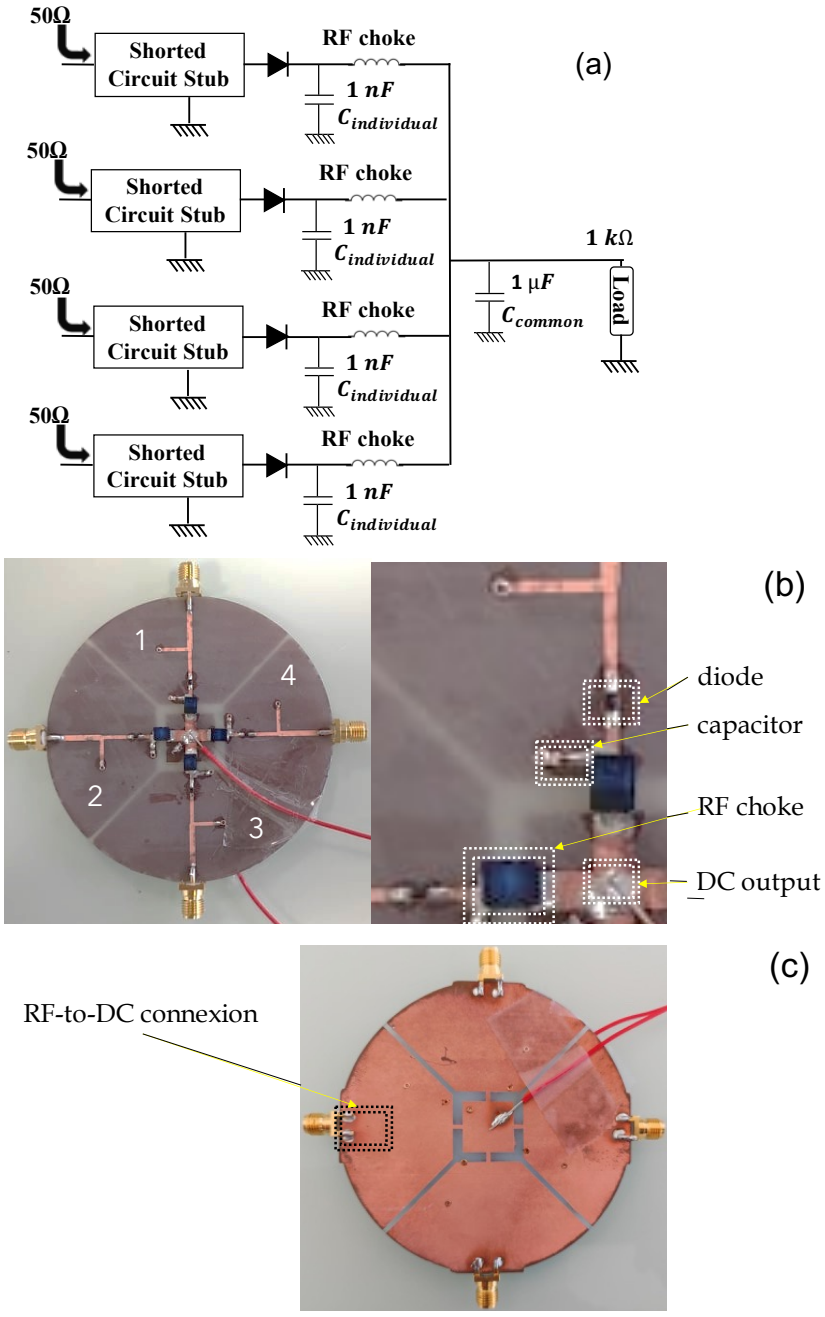

Figure 8. 4 complementary rectifiers. (**a**) Electrical circuit. (**b**) Experimental vehicle (top face). (**c**) Bottom face.

The approach in Figure 7 is applied to characterize the open-circuit voltage and the conversion efficiency at −10 dBm input RF power and for various rectenna configurations (namely the number of antenna stimulated at the same time or the output load value). The rectifier substrate is printed in HT resin V2. In the case where two rectifier inputs are supplied simultaneously with −10 dBm and the other ports short-circuited on 50 Ω (Figure 9), the conversion efficiency is over 10% at an optimal load of 1.2 kΩ. In [58] it appears that the internal impedance of a sector-rectenna is nearly 2010 Ω. Unfortunately the authors do not detail how the DC paths are combined to supply a unique load. The available DC power is then 10 mW under 65 mV. A voltage conversion circuit is necessary, but the available power becomes highly compatible with IoT object power consumption.

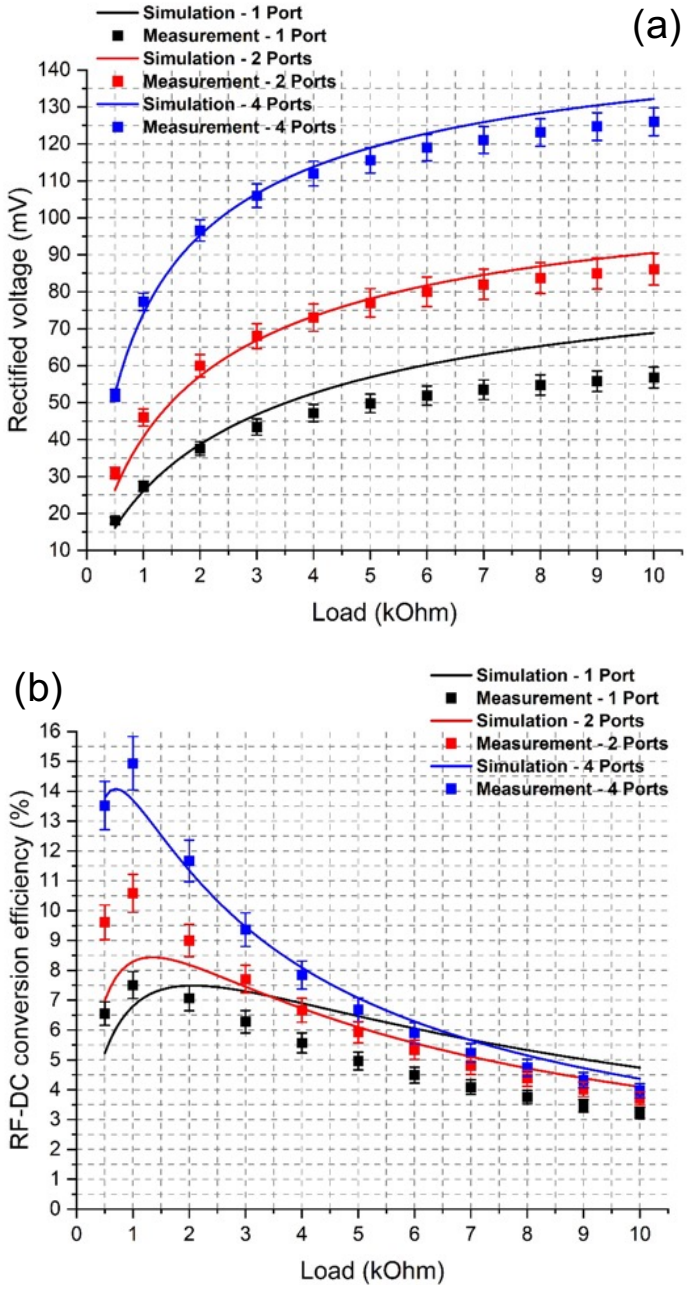

Figure 9. 4 complementary rectifier circuit in HT resin V2. (**a**) Output voltage at −10 dBm input RF power. (**b**) Conversion efficiency at −10 dBm input RF power.

One important detail is that the excitation of the circularly polarized patch antenna by the ambient electromagnetic field is generally unknown and is varying in time. It is not reasonable to install a circuit to sense individually the DC output of each rectenna in Figure 8 to correct the instantaneous optimal load of the system. Hence, a constant value of near-optimal load must be identified. The near-optimal load is identified in the conversion efficiency curve of the rectenna system for a given configuration of ambient electromagnetic field (i.e., which antenna is polarized and which input RF power level is applied at the related rectifier input). A Design-of-Experiment (DoE) with 69 cases is considered: the total input RF power level at the rectifier input is [−30 dBm; −20 dBm; −10 dBm and 0 dBm] and each of the 4 possible rectifier ports are considered independently (i.e., leading to cases where ports are not receiving the same input power).

The near-optimal load identification is pictured in Figure 10. The DoE indicates that 1 kΩ will act as a near-optimal or closely-optimal load value in a number of cases. This value is selected as a specification for the voltage conversion block. It is clear that over time the operation of the rectenna will not be optimal in the perspective of maximum power point. There is a trade-off regarding the load value and regarding the maximum harvested energy over a time horizon.

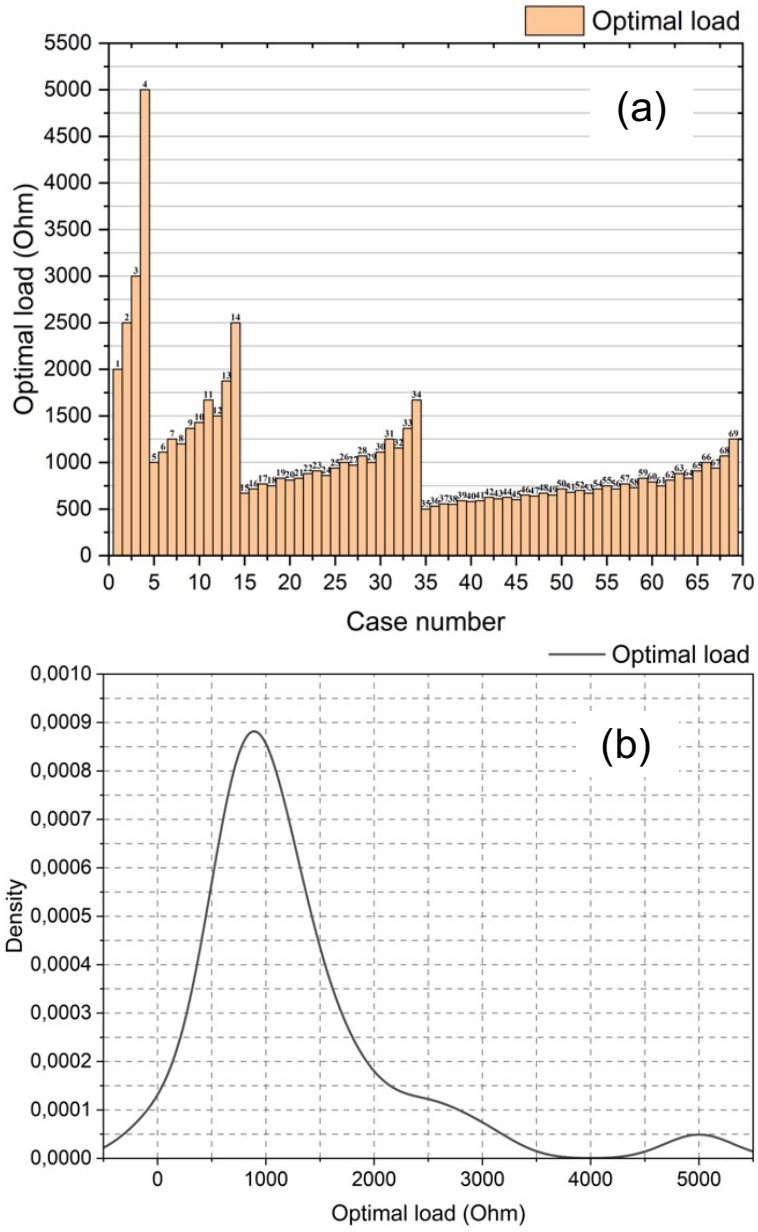

Figure 10. Design-of-Experiment for identifying an effective value of near-optimal load. (**a**) Histogram of 69 results. (**b**) Conversion efficiency at −10 dBm input RF power level.

5. Voltage Conversion Circuit

This Section details a lab-scale voltage conversion circuit that should load the rectenna with a near-optimal load of 1 kΩ and supply an output DC load between 1.5 V and 1.9 V. As the RF power density at the antenna surface is low and lower than the energy required by an IoT sensor over an operating cycle, it is necessary to store the electrical energy.

Several commercial circuits exist to deal with the voltage conversion from energy harvesting (Table 7). These circuits do not answer to the critical trade-off of accepting

a micro-voltage source with a high internal impedance (1 kΩ), starting-up at the lowest possible voltage, and consuming a low bias current.

Table 7. Popular voltage conversion circuits dedicated to RFEH.

	Cold Start Voltage (mV)	bias Current
BQ25504 [64]	>600	<0.33 µA at 2.2 V (0.726 µW)
AEM30940 [65]	380	<0.875 µA at 3.7 V (3.23 µW)
LTC3108 [66]	20	0.2 µA at 3.3 V (0.66 µW)
[67]	2000	0.15 µA at 3 V (0.45 µW)
[68]	1950	0.2 µA at 1.95 V (0.39 µW)
[69]	300	1.56 µA at 2 V (3.12 µW)
This work	180	4.2 µA at 1.4 V (5.8 µW)

A voltage conversion circuit was proposed in [70] to deal with the large internal impedance of the rectenna and cold-starting at the minimum voltage of 180 mV (Figure 11). The circuit was improved in [71] to deal with a 100 µW micro-voltage source. The main converter in Figure 11 is a Flyback DC-DC converter operating in discontinuous conduction mode (DCM). It was demonstrated in [71] that the input impedance, R_{in}, of the Flyback is defined in a straight-forward manner as follows:

$$R_{in} = \frac{2Lf}{d^2} = 1\,\text{k}\Omega \rightarrow Lf = 125\,\text{H.Hz}, \quad (1)$$

where L is the magnetizing inductance of the coupled-inductance device, f is the switching frequency and d is the duty cycle (50% in most cases). Given component references and considering an ideal coupled-inductance magnetic device, it is possible to build the abacus in Figure 12 to show the trade-off between the efficiency and the size of the magnetic device. When crossing this abacus with the commercial magnetic device offer, the designer sets the efficiency of the Flyback converter as well as its size. The size may be bulky if a large magnetizing inductance is selected with a low series resistance, i.e., a large number of winding turns with a large section conductor. Besides, popular integrated circuits in Table 7 offer a better trade-off in terms of size, but the cold start-up voltage must be higher than the one of the lab-scale converter or the integrated maximum power-point tracking algorithm will definitely not be adapted to a RFEH. The emerging commercial circuit [65] is one of the most appropriate offers as of today to the best knowledge of the authors, if a high integration factor is sought.

The circuit in Figure 11 is implemented with the list of devices in Table 8. It is verified experimentally that the Amstrong part is capable of starting-up for an input DC voltage of 180 mV. The integrated circuit LTC3108 [66] in Table 7 is capable of wake-up under 20 mV, but only for a low internal voltage source. This is not applicable to a RFEH.

Table 8. List of components in the circuit in Figure 11a.

Amstrong	Transformer, MT1 WE750311681	n-JET, J1 J201	p-JFET, J2 J177	Diode, D1 BAT54
Flyback	Transformer, MT2 LPD6235-205	Oscillator TS3002	nMOS, M1 FDV301N	Diode, D2 BAT54
Under Voltage Lock-Out	nMOS, M2-M5 FDV301N	pMOS, P1-P2 FDV304P		

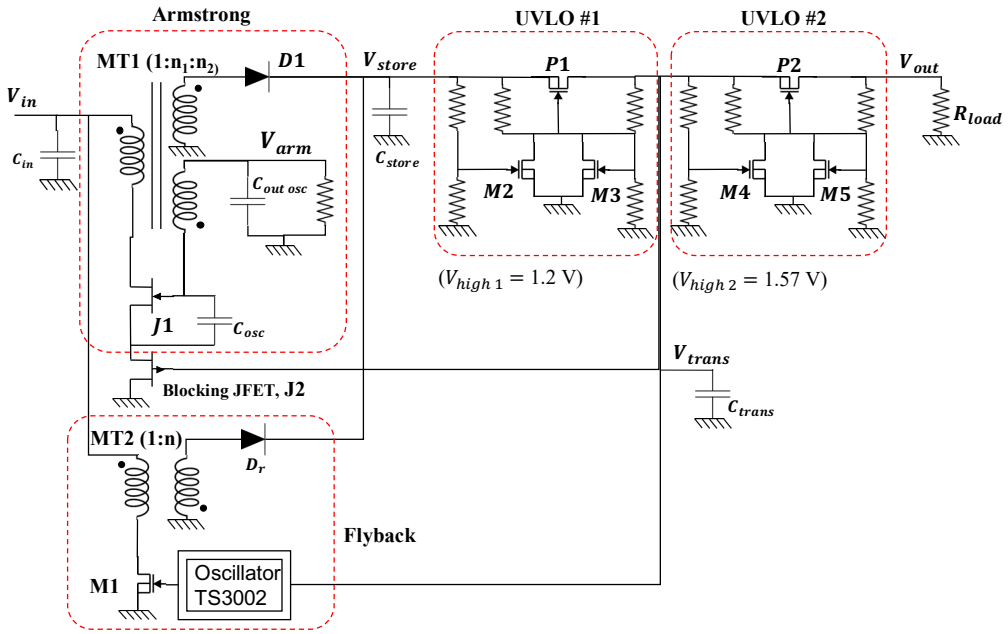

Figure 11. Schematic of voltage conversion circuit for a rectenna.

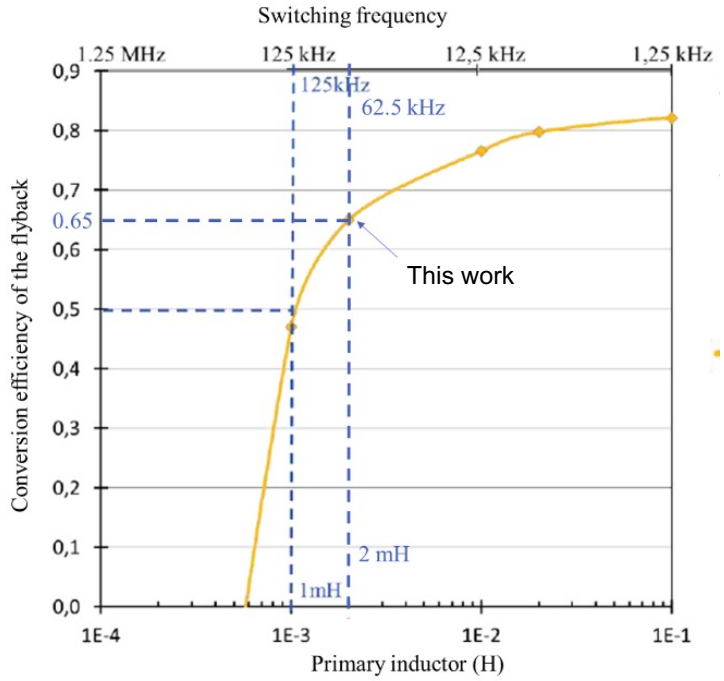

Figure 12. Abacus of efficiency of the Flyback in Figure 11 with respect to Equation (1).

Under −20 dBm input RF power, the rectifier delivers nearly 0.5 V in open-circuit condition. The Amstrong converter efficiency is 40.2%. It takes less than 3 s to charge a 47 µF under 1.4 V. The Flyback efficiency is measured at 73% for a load of 100 kΩ, excluding the bias current of the oscillator (TS3002). The TS3002 oscillator draws 4 µJ in normal operating conditions. The UVLO blocks consume a negligible energy. The net output power of the voltage conversion circuit is more than 7.2 µW at −20 dBm input RF power. It will then take nearly 14 s to store 100 µJ in the output capacitive buffer. As will be discussed later on, supplying an IoT sensor will lead to a sporadic operation if the IoT's consumption is too high or the input RF power drops in level and the Flyback cannot operate any further. The Flyback is able to operate with an input DC voltage as low as 100 mV, i.e., 10 µW.

6. System-Level Measurements and Discussion

The near-circular polarization patch antenna vehicle is illuminated by a calibrated patch antenna, so as to receive −10 dBm in the antenna plane. The four-rectenna system is connected to the voltage converter and a resistor emulates a consumption load (Figure 13).

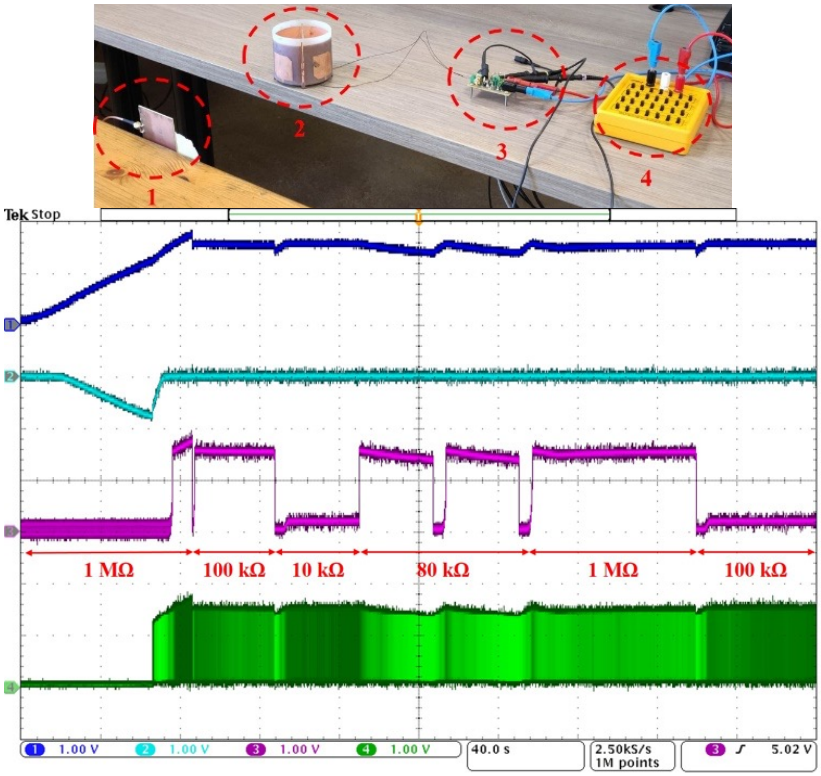

Figure 13. Evaluation of the rectenna vehicle operation at 2.45 GHz. (**top**) test setup (1-emitting patch; 2-circular antenna; 3-voltage converter; 4-load). (**bottom**) main waveforms of voltages in the circuit in Figure 11a (blue: V_{store}; light blue: V_{arm}; purple: V_{out}; green: V_{osc}).

6.1. Results in Normal Operating Mode

The rectenna delivers 0.26 V open-circuit voltage to the voltage converter. The Amstrong part of the converter starts-up and begins charging the primary capacitive buffer (first 72 s, voltage V_{store}). At t = 72 s, the UVLO #1 turns on. The oscillator TS3002 controlling the Flyback is supplied and the output capacitive buffer is connected to the primary one. The Flyback puts the Amstrong oscillator in idle mode (voltage V_{arm} gets back to zero) and charges some more the capacitors. At 76 s the UVLO #2 turns on and the load is supplied. When the load is 1 MΩ, the output voltage, V_{out}, reaches a steady-state. The energy inflow is higher than the one consumed by the large load. The output voltage keeps rising along with the charge of the capacitors. At 84 s, the load is changed to 100 kΩ. There is nearly a balance between the harvested energy and the load consumption (25.6 µW). A load of 10 kΩ is excessive and drains quite aggressively the capacitive buffer (at 124 s). The UVLO #2 turns off immediately and the Flyback charges the capacitors again, as the DC input voltage is higher than 100 mV. When the load is 80 kΩ, the capacitive buffers are able to offer a supply for 24 s. The output voltage decreases linearly because of the constant output current. Nearly 51 µJ are delivered to the load. It takes 3 s to the Flyback to deliver back this amount of energy to the capacitors.

6.2. Discussion

A comparison between the experimental results regarding the circularly polarized patch antenna vehicle and the ones in the state of the art is shown in Table 9. The selected references are related to patch antennas operating at 2.45 GHz. An antenna design on

Rogers substrate in [72] exhibits a lower gain because of a thinner substrate. The HT resin v1 substrate yields similar results as FR4 [73] because of nearly similar dielectric parameters. The proposed antenna vehicle in HT resin v2 is comparable to the one in [74]. The antenna introduced in [75] offers a better gain, even if the conductor has a lower conductivity. This can be explained by the larger substrate thickness and lower tanδ. As a conclusion, the rapid prototyping of a patch antenna array on a printed polymer substrate is valuable, not optimal, but significant so far. Rogers Company has recently patented a polymer composition for the 3D stereolithography printing of RF substrates [55]. The patent announces a feasible 3D substrate with very low losses (as low as 0.01). A margin for improvement is then foreseeable.

Table 9. Comparison with state-of-the-art antennas for RFEH at 2.45 GHz.

	Substrate (ϵ_r, tan(δ))	**Observation**	**Antenna**	**Meas. Gain (dBic)**	**Size (mm^3)**
[73]	FR-4 (4.3, 0.02)		Fractal patch	2.72	26.4 × 26.4 × 1.6
[72]	Rogers 4003C (3.55, 0.0021)		Patch	5	32 × 31.5 × 0.83
[74]	Felt (1.3, 0.044)	170 µm-thick ShieldIt conductive fabric (8.47 µΩ·m)	Reconfigurable patch	2–3.9	46.5 × 39 × 3.3
[74]	VeroWhite	Inkjet printing/20 µm-thick silver nanoparticles ink then diammine-silver acetate ink (0.2 µΩ·m)	Patch	4–4.2	27.9 × 35.9 × 3
This work	Rogers 4003C (3.55, 0.0021)	Laminated copper	Patch	5.3	32 × 56.1 × 1.5
	HT Resin v1 (3, 0.025)	EDL copper (0.02–0.025 µΩ·m)	Patch	2.5	36.1 × 57.15 × 1.5
	HT Resin v2 (2.9, 0.04)	EDL copper	Curved patch (Common ground)	1.26	36 × 43 × 1.5
	HT Resin v2	ELD copper	Curved patch (Segmented ground)	1.6	36 × 43 × 1.5

As an example of an IoT object, we consider an hypothetical system made of a low-power temperature sensor STTS22H from STMicroelectronics operated by a low-power microcontroller RF430FRL152H from Texas Instruments. The wireless communications towards a gateway would be inferred by a Bluetooth chip like IS1871SF-202-TRAY from Microchip. This system can be considered as the low-end devices of IoT [76], quite representative of the variety of existing IoT platforms [77]. From the various datasheets, it appears that the sensor would operate over a 120 ms cycle. The sensing part of the cycle consumes an average current of 280 µA under 1.5 V and during 119 ms. The communication part consumes 10 mA under 1.9 V and during 1 ms. It is a simplified view of the system operation for straight quantification of electrical energy balance. As an example, a detailed analysis of a realistic system may be found in [78].

The energy budget is then 49.6 µJ over 119 ms and 19 µJ over 1 ms. Two capacitors are necessary but the circuit in Figure 11 is nearly able to provide two voltage levels, providing a slight modification of the circuit and a correct tuning of UVLO blocks. Introducing two DC voltage levels does not mean more complexity. If a net capacitor voltage variation

of 5% is tolerated during operation, then devices of 440 µF @ 1.5 V and 100 µF @ 1.9 V, respectively. The net flow of energy per cycle is 68.6 µJ over 120 ms. RFEH may offer a net flow of energy of the same order of magnitude but fail to consider ambient electromagnetic energy. With proper tuning of UVLO thresholds, the voltage converter above is able to deliver the amount of energy. Under −10 dBm of input RF power at the rectenna input, capturing the energy that is in the capacitive buffer requires 3 s. The IoT system may not operate continuously and the ratio of sporadic operation is $\frac{120\text{ ms}}{3\text{ s}} = 4\%$.

Indeed, the natural ambient RF energy is less than -30 dBm on the remarkable frequency band. It is not possible to supply an IoT device comprising a sensor, a microcontroler and a wireless communication at the same time. This is why most applications detailed in the literature operate with input RF power above −10 dBm. In [79], it is proposed to couple two energy paths: an RFEH is dedicated to ambient RF energy and supplies essentially the sensor and minimal operation of the microcontroler, while a Wireless Power Transfer (WPT) link is dedicated to communication. When dealing with input RF power larger than −30 dBm, the RF energy comes from an active emission or WPT. The proposed vehicle here was meant to demonstrate that additive manufacturing is not a killer of RFEH. The presented circularly polarized antenna, rectifier and voltage conversion system operate with an input RF power above −13.5 dBm, necessary to provide the minimum cold starting DC voltage to the voltage conversion circuit. Under −10 dBm, the global efficiency is 14.8%. An IoT object with a large effective skin surface will accommodate an antenna with a larger gain and the minimum operating input RF power will be at a lower level.

7. Conclusions

This paper wishes to demonstrate that the polymer considered for additive manufacturing of IoT objects may be also used to incorporate an RFEH capability into the object, thanks to a proper process, such as the 3D Plastronics rapid prototyping. The dielectric parameters of most common printable polymers are not optimal for RF functions, at least while waiting for a Rogers Company new resin, as announced in a recent patent. However, a simple resonant patch antenna may be designed and offers decent performances. The antenna geometry may match the one of the IoT object surface skin. An RF-to-DC rectifier may also be considered and offers a fair output impedance and a conversion efficiency that authorizes an effective energy harvesting. A lab-scale voltage converter circuit was evaluated to obtain the order of magnitude of DC energy necessary to supply an IoT (tiny) system for a certain amount of time. The system may operate in the condition of quite low RF power, but not in a continuous manner. Obviously and from a general point-of-view, an RFEH capability should be reserved to IoT systems with sporadic operation.

Author Contributions: Methodology, J.V.; Validation, J.-M.D. and P.B. (Philippe Benech); Investigation, X.V.L.N., T.G. and P.L.; Resources, P.B. (Pascal Bevilacqua); Data curation, P.U.L. and F.M.; Writing—original draft, B.A.; Project administration, M.C. All authors have read and agreed to the published version of the manuscript.

Funding: This research was funded by project IPCEI Nano 2022—INCA.

Institutional Review Board Statement: Not applicable.

Informed Consent Statement: Not applicable.

Data Availability Statement: Not applicable.

Acknowledgments: The authors wish to thank the support of Region Auvergne-Rhone-Alpes regarding 3D Plastronics within the COMSUP program.

Conflicts of Interest: The authors declare no conflict of interest.

Abbreviations

The following abbreviations are used in this manuscript:

RFEH	Radio-Frequency Energy Harvester
SLA	3D stereolithography printing method
ELD	Electroless copper deposition Layer method
TTL	Two Transmission Lines method

References

1. Mouapi, A. Radiofrequency Energy Harvesting Systems for Internet of Things Applications: A Comprehensive Overview of Design Issues. *Sensors* **2022**, *22*, 8088. [CrossRef] [PubMed]
2. Bahhar, C.; Baccouche, C.; Sakli, H. Millimeter-Wave Rectenna and Rectifying Circuits for Wireless Power Transfer in 60 GHz. In Proceedings of the 2022 19th International Multi-Conference on Systems, Signals & Devices (SSD), Sétif, Algeria, 6–10 May 2022; pp. 1346–1350. [CrossRef]
3. Gu, X.; Guo, L.; Hemour, S.; Wu, K. Optimum Temperatures for Enhanced Power Conversion Efficiency (PCE) of Zero-Bias Diode-Based Rectifiers. *IEEE Trans. Microw. Theory Tech.* **2020**, *68*, 4040–4053. [CrossRef]
4. Nguyen, X.V.L.; Gerges, T.; Duchamp, J.M.; Benech, P.; Verdier, J.; Lombard, P.; Cabrera, M.; Allard, B. 3D Plastronics Radio Frequency Energy Harvester on Stereolithography Parts. In Proceedings of the 2022 Wireless Power Week (WPW), Bordeaux, France, 5–8 July 2022; pp. 156–161. [CrossRef]
5. Khonsari, Z.; Björninen, T.; Tentzeris, M.M.; Sydänheimo, L.; Ukkonen, L. 2.4 GHz inkjet-printed RF energy harvester on bulk cardboard substrate. In Proceedings of the 2015 IEEE Radio and Wireless Symposium (RWS), San Diego, CA, USA, 25–28 January 2015; pp. 153–155, ISSN 2164-2974. [CrossRef]
6. Nguyen, D.A.; Bui, G.T.; Nam, H.; Seo, C. Design of Dual-Band Inverse Class-F Rectifier for Wireless Power Transfer and Energy Harvesting. *IEEE Microw. Wirel. Components Lett.* **2022**, 1–4. [CrossRef]
7. Stoopman, M.; Keyrouz, S.; Visser, H.J.; Philips, K.; Serdijn, W.A. Co-Design of a CMOS Rectifier and Small Loop Antenna for Highly Sensitive RF Energy Harvesters. *IEEE J. Solid-State Circuits* **2014**, *49*, 622–634. [CrossRef]
8. Palazzi, V.; Hester, J.; Bito, J.; Alimenti, F.; Kalialakis, C.; Collado, A.; Mezzanotte, P.; Georgiadis, A.; Roselli, L.; Tentzeris, M.M. A Novel Ultra-Lightweight Multiband Rectenna on Paper for RF Energy Harvesting in the Next Generation LTE Bands. *IEEE Trans. Microw. Theory Tech.* **2018**, *66*, 366–379. [CrossRef]
9. Eid, A.; Costantine, J.; Tawk, Y.; Ramadan, A.H.; Abdallah, M.; Elhajj, R.; Awad, R.; Kasbah, I.B. An efficient RF energy harvesting system. In Proceedings of the 2017 11th European Conference on Antennas and Propagation, EUCAP, Paris, France, 19–24 March 2017; pp. 896–899. [CrossRef]
10. Liu, Z.; Li, Z.; Li, J.; Xiao, P.; Qiu, Y.; Li, G.; Ho, J.S. A Body-Wide RF Energy Harvester Based on Textile Surface Plasmonic Antenna Array for Wearable Wireless Power Transmission. *IEEE Trans. Circuits Syst. II Express Briefs* 2022, *early access*. [CrossRef]
11. Calignano, F.; Manfredi, D.; Ambrosio, E.P.; Biamino, S.; Lombardi, M.; Atzeni, E.; Salmi, A.; Minetola, P.; Iuliano, L.; Fino, P. Overview on Additive Manufacturing Technologies. *Proc. IEEE* **2017**, *105*, 593–612. [CrossRef]
12. Chen, Y.; Zhang, C.; Lu, Y.; Yang, W.W.; Huang, J. Compact Dual-Polarized Base Station Antenna Array Using Laser Direct Structuring Technique. *IEEE Antennas Wirel. Propag. Lett.* **2021**, *20*, 78–82. [CrossRef]
13. Bengloan, G.; Froppier, B.; Chousseaud, A.; Girard, J.; Cruz, E.M. Plastronics Development of Low-Profile Conformal Antenna for IoT Sensors. In Proceedings of the 2021 15th European Conference on Antennas and Propagation (EuCAP), Dusseldorf, Germany, 22–26 March 2021; pp. 1–5. [CrossRef]
14. Muhammad, S.; Tiang, J.J.; Wong, S.K.; Smida, A.; Ghayoula, R.; Iqbal, A. A Dual-Band Ambient Energy Harvesting Rectenna Design for Wireless Power Communications. *IEEE Access* **2021**, *9*, 99944–99953. [CrossRef]
15. Song, C.; Huang, Y.; Zhou, J.; Zhang, J.; Yuan, S.; Carter, P. A High-Efficiency Broadband Rectenna for Ambient Wireless Energy Harvesting. *IEEE Trans. Antennas Propag.* **2015**, *63*, 3486–3495. [CrossRef]
16. Bakytbekov, A.; Nguyen, T.Q.; Huynh, C.; Salama, K.N.; Shamim, A. Fully printed 3D cube-shaped multiband fractal rectenna for ambient RF energy harvesting. *Nano Energy* **2018**, *53*, 587–595. [CrossRef]
17. Linh Nguyen, X.V.; Gerges, T.; Duchamp, J.M.; Benech, P.; Verdier, J.; Lombard, P.; Cabrera, M.; Allard, B. Stereolithography-Based Rectenna for Wireless Energy Harvesting. In Proceedings of the 2021 IEEE 34th International System-on-Chip Conference (SOCC), Las Vegas, NV, USA, 14–17 September 2021; pp. 34–39, ISSN 2164-1706. [CrossRef]
18. Georgiadis, A.; Collado, A.; Via, S.; Meneses, C. Flexible hybrid solar/EM energy harvester for autonomous sensors. In Proceedings of the 2011 IEEE MTT-S International Microwave Symposium, Baltimore, MD, USA, 5–10 June 2011; pp. 1–4, ISSN 0149-645X. [CrossRef]
19. Awais, Q.; Jin, Y.; Chattha, H.T.; Jamil, M.; Qiang, H.; Khawaja, B.A. A Compact Rectenna System With High Conversion Efficiency for Wireless Energy Harvesting. *IEEE Access* **2018**, *6*, 35857–35866. [CrossRef]
20. Sun, H.; Guo, Y.-X.; He, M.; Zhong, Z. A dual-band rectenna using broadband yagi antenna array for ambient rf power harvesting. *IEEE Antennas Wirel. Propag. Lett.* **2013**, *12*, 918–921. [CrossRef]

21. Gu, X.; De Almeida, J.V.; Hemour, S.; Khazaka, R.; Wu, K. Thermal Effects on Low-Power RF-to-dc Voltage Multiplier for Battery-Free Sensing and IoT. In Proceedings of the 2022 Wireless Power Week (WPW), Bordeaux, France, 5–8 July 2022; pp. 29–32. [CrossRef]
22. Hamidouche, A.M.; Takhedmit, H.; Poulichet, P.; Cirio, L. Efficiency improvement of an UWB rectifier by using optimized pulse modulation signal: Simulation and experiments. In Proceedings of the 2022 Wireless Power Week (WPW), Bordeaux, France, 5–8 July 2022; pp. 407–411. [CrossRef]
23. Biswas, A.; Babak Hamidi, S.; Biswas, C.; Roy, P.; Mitra, D.; Dawn, D. A novel CMOS RF energy harvester for self-sustainable applications. In Proceedings of the 2018 IEEE 19th Wireless and Microwave Technology Conference (WAMICON), Sand Key, FL, USA, 9–10 April 2018; pp. 1–5. [CrossRef]
24. Muramoto, Y.; Sakai, N.; Itoh, K. A 920 MHz band rectenna with the impedance transfomed small loop antenna (IT-SLA). In Proceedings of the 2022 Wireless Power Week (WPW), Bordeaux, France, 5–8 July 2022; pp. 400–403. [CrossRef]
25. Niotaki, K.; Kim, S.; Jeong, S.; Collado, A.; Georgiadis, A.; Tentzeris, M.M. A Compact Dual-Band Rectenna Using Slot-Loaded Dual Band Folded Dipole Antenna. *IEEE Antennas Wirel. Propag. Lett.* **2013**, *12*, 1634–1637. [CrossRef]
26. Khalid, F.; Saeed, W.; Shoaib, N.; Khan, M.U.; Cheema, H.M. Quad-Band 3D Rectenna Array for Ambient RF Energy Harvesting. *Int. J. Antennas Propag.* **2020**, *2020*, e7169846. [CrossRef]
27. Shen, S.; Chiu, C.Y.; Murch, R.D. A Dual-Port Triple-Band L-Probe Microstrip Patch Rectenna for Ambient RF Energy Harvesting. *IEEE Antennas Wirel. Propag. Lett.* **2017**, *16*, 3071–3074. [CrossRef]
28. Nikkhah, N.; Keshavarz, R.; Abolhasan, M.; Lipman, J.; Shariati, N. Efficient Dual-Band Single-Port Rectifier for RF Energy Harvesting at FM and GSM Bands. In Proceedings of the 2022 Wireless Power Week (WPW), Bordeaux, France, 5–8 July 2022; pp. 141–145. [CrossRef]
29. Phan, K.T.; Le-Ngoc, T. Power Allocation for Buffer-Aided Full-Duplex Relaying with Imperfect Self-Interference Cancelation and Statistical Delay Constraint. *IEEE Access* **2016**, *4*, 3961–3974. [CrossRef]
30. Lin, C.H.; Chiu, C.W.; Gong, J.Y. A Wearable Rectenna to Harvest Low-Power RF Energy for Wireless Healthcare Applications. In Proceedings of the 2018 11th International Congress on Image and Signal Processing, BioMedical Engineering and Informatics (CISP-BMEI), Beijing, China, 13–15 October 2018; pp. 1–5. [CrossRef]
31. Mansour, M.M.; Kanaya, H. Compact RF rectifier circuit for ambient energy harvesting. In Proceedings of the 2017 IEEE International Symposium on Radio-Frequency Integration Technology (RFIT), Seoul, Republic of Korea, 30 August–1 September 2017; pp. 220–222. [CrossRef]
32. Ur Rehman, M.; Ahmad, W.; Khan, W.T. Highly efficient dual band 2.45/5.85 GHz rectifier for RF energy harvesting applications in ISM band. In Proceedings of the 2017 IEEE Asia Pacific Microwave Conference (APMC), Kuala Lumpur, Malaysia, 13–16 November 2017; pp. 150–153. [CrossRef]
33. Tafekirt, H.; Pelegri-Sebastia, J.; Bouajaj, A.; Reda, B.M. A Sensitive Triple-Band Rectifier for Energy Harvesting Applications. *IEEE Access* **2020**, *8*, 73659–73664. [CrossRef]
34. Almoneef, T.S. Design of a Rectenna Array without a Matching Network. *IEEE Access* **2020**, *8*, 109071–109079. [CrossRef]
35. Eid, A.; Hester, J.G.D.; Costantine, J.; Tawk, Y.; Ramadan, A.H.; Tentzeris, M.M. A Compact Source–Load Agnostic Flexible Rectenna Topology for IoT Devices. *IEEE Trans. Antennas Propag.* **2020**, *68*, 2621–2629. [CrossRef]
36. Papadopoulou, M.S.; Boursianis, A.D.; Volos, C.K.; Stouboulos, I.N.; Nikolaidis, S.; Goudos, S.K. High-Efficiency Triple-Band RF-to-DC Rectifier Primary Design for RF Energy-Harvesting Systems. *Telecom* **2021**, *2*, 271–284. [CrossRef]
37. Aboualalaa, M.; Mansour, I.; Mansour, M.; Bedair, A.; Allam, A.; Abo-Zahhad, M.; Elsadek, H.; Yoshitomi, K.; Pokharel, R.K. Dual-band Rectenna Using Voltage Doubler Rectifier and Four-Section Matching Network. In Proceedings of the 2018 IEEE Wireless Power Transfer Conference (WPTC), Montreal, QC, Canada, 3–7 June 2018; pp. 1–4. [CrossRef]
38. Mouapi, A.; Hakem, N.; Kandil, N.; Kamani, G.V. A Miniature Rectifier Design for Radio Frequency Energy Harvesting Applied at 2.45 GHz. In Proceedings of the 2018 IEEE International Conference on Environment and Electrical Engineering and 2018 IEEE Industrial and Commercial Power Systems Europe (EEEIC/I&CPS Europe), Palermo, Italy, 12–15 June 2018; pp. 1–5. [CrossRef]
39. Asakura, S.; Yamanokuchi, S.; Yoshida, S.; Nishikawa, K. Design and Prototyping of a Single-Shunt Rectifier with 71% Fractional Bandwidth Having Acceptable Matching on 10 dBm LSSP. In Proceedings of the 2022 Wireless Power Week (WPW), Bordeaux, France, 5–8 July 2022; pp. 383–387. [CrossRef]
40. Hoque, M.U.; Kumar, D.; Audet, Y.; Savaria, Y. Design and Analysis of a 35 GHz Rectenna System for Wireless Power Transfer to an Unmanned Air Vehicle. *Energies* **2022**, *15*, 320. [CrossRef]
41. Bhatt, C.R.; Henderson, S.; Brzozek, C.; Benke, G. Instruments to measure environmental and personal radiofrequency-electromagnetic field exposures: An update. *Phys. Eng. Sci. Med.* **2022**, *45*, 687–704. [CrossRef] [PubMed]
42. Zhao, J.; Ghannam, R.; Htet, K.O.; Liu, Y.; kay Law, M.; Roy, V.A.; Michel, B.; Imran, M.A.; Heidari, H. Self-Powered Implantable Medical Devices: Photovoltaic Energy Harvesting Review. *Adv. Healthc. Mater.* **2020**, *9*, 2000779. [CrossRef] [PubMed]
43. Wang, D.; Chang, K. Electromagnetic energy harvesting from flow induced vibration. *Microelectron. J.* **2010**, *41*, 356–364. [CrossRef]
44. Wang, M.; Chen, J.; Cui, X.; Li, L. Design and Fabrication of 5.8GHz RF Energy Harvesting Rectifier. In Proceedings of the 2019 Cross Strait Quad-Regional Radio Science and Wireless Technology Conference, CSQRWC, Taiyuan, China, 18–21 July 2019; pp. 1–3. [CrossRef]

45. Kawai, K.; Takabayashi, N.; Toyonaga, T.; Suzuki, K.; Shinohara, N. Development of Rectenna for Estimating Received Power Level Using Second Harmonic Wave. In Proceedings of the 2022 Wireless Power Week (WPW), Bordeaux, France, 5–8 July 2022; pp. 175–179. [CrossRef]
46. Gerges, T.; Semet, V.; Lombard, P.; Gaillard, S.; Cabrera, M.; Lambert, S.A. 3D Plastronics for Smartly Integrated Magnetic Resonance Imaging Coils. *Front. Phys.* **2020**, *8*, 240. [CrossRef]
47. Franke, J. *Three-Dimensional Molded Interconnect Devices (3D-MID)*; Hanser: Munich, Germany, 2014; pp. I–XII. [CrossRef]
48. IPC—The Global Association for Electronics Manufacturing. 2022. Available online: www.ipc.org (accessed on 15 December 2022).
49. Acharya, S.; Chouhan, S.S.; Delsing, J. Fabrication Process for On-Board Geometries Using a Polymer Composite-Based Selective Metallization for Next-Generation Electronics Packaging. *Processes* **2021**, *9*, 1634. [CrossRef]
50. Gerges, T.; Marie, A.; Wickramasinghe, T.; Lombard, P.; Levêque, M.; Lips, S.; Sartre, V.; Allard, B.; Cabrera, M. Investigation of 3D printed polymer-based heat dissipator for GaN transistors. In Proceedings of the 2021 23rd European Conference on Power Electronics and Applications (EPE'21 ECCE Europe), Ghent, Belgium, 6–10 September 2021; pp. P.1–P.9. [CrossRef]
51. Walterpack Company. Plastronics: Electronics Meets Plastic. 2022. Available online: https://www.walterpack.com/de/plastronics-electronics-meets-plastic-2/ (accessed on 15 December 2022).
52. Adams, J.J.; Duoss, E.B.; Malkowski, T.F.; Motala, M.J.; Ahn, B.Y.; Nuzzo, R.G.; Bernhard, J.T.; Lewis, J.A. Conformal Printing of Electrically Small Antennas on Three-Dimensional Surfaces. *Adv. Mater.* **2011**, *23*, 1335–1340. [CrossRef]
53. Formlabs. Guide to Stereolithography (SLA) 3D Printing. 2022. Available online: https://formlabs.com (accessed on 15 December 2022).
54. Baker-Jarvis, J.; Janezic, M.D.; Degroot, D.C. High-frequency dielectric measurements. *IEEE Instrum. Meas. Mag.* **2010**, *13*, 24–31. [CrossRef]
55. Polidore, T.; Baars, D.; Koes, T.A.; Fitts, B.; Sethumadhavan, M. Photocurable Compositions for Stereolithography, Stereolithography Methods Using the Compositions, Polymer Components Formed by the Stereolithography Methods, and a Device Including the Polymer Components. WO Patent WO 2020/243429 A1, 3 December 2020.
56. Balanis, C. *Antenna Theory: Analysis and Design*, 4th ed.; Wiley: Hoboken, NJ, USA, 2016.
57. Niamien, C.M.A. Optimum Antenna Characteristics for Maximally Harvesting Ambient RF Energy. *IEEE Open J. Antennas Propag.* **2022**, *3*, 1364–1381. [CrossRef]
58. Kumar, M.; Kumar, S.; Sharma, A. An Analytical Framework of Multisector Rectenna Array Design for Angular Misalignment Tolerant RF Power Transfer Systems. *IEEE Trans. Microw. Theory Tech.* **2022**, 1–13. [CrossRef]
59. Vandelle, E.; Bui, D.H.N.; Vuong, T.P.; Ardila, G.; Wu, K.; Hemour, S. Harvesting Ambient RF Energy Efficiently with Optimal Angular Coverage. *IEEE Trans. Antennas Propag.* **2019**, *67*, 1862–1873. [CrossRef]
60. Hemour, S.; Zhao, Y.; Lorenz, C.H.P.; Houssameddine, D.; Gui, Y.; Hu, C.M.; Wu, K. Towards Low-Power High-Efficiency RF and Microwave Energy Harvesting. *IEEE Trans. Microw. Theory Tech.* **2014**, *62*, 965–976. [CrossRef]
61. Muntoni, G.; Montisci, G.; Casula, G.A.; Chietera, F.P.; Michel, A.; Colella, R.; Catarinucci, L.; Mazzarella, G. A Curved 3-D Printed Microstrip Patch Antenna Layout for Bandwidth Enhancement and Size Reduction. *IEEE Antennas Wirel. Propag. Lett.* **2020**, *19*, 1118–1122. [CrossRef]
62. Geng, J.P.; Li, J.; Jin, R.H.; Ye, S.; Liang, X.; Li, M. The deveopment of curved microstrip antenna with defected ground structure. *Prog. Electromagn. Res.* **2009**, *98*, 53–73. [CrossRef]
63. Gonzalez, M. Analysis of Conformal Antennas for Avionics Applications. Ph.D. Thesis, Chalmers University of Technology, Gothenburg, Sweden, 2007.
64. Texas Instruments. BQ25504 Ultra Low-Power Boost Converter with Battery Management for Energy Harvester Applications. Available online: https://www.ti.com/lit/ds/symlink/bq25504.pdf (accessed on 15 December 2022).
65. E-PEAS Semiconductors. Energy Harvesting Batery Chargers for Simple Integration. Available online: https://e-peas.com/product/aem30940/ (accessed on 15 December 2022).
66. Analog Devices. Ultralow Voltage Step-Up Converter and Power Manager. Available online: https://www.analog.com/en/products/ltc3108.html#product-overview (accessed on 15 December 2022).
67. Adami, S.E.; Proynov, P.; Hilton, G.S.; Yang, G.; Zhang, C.; Zhu, D.; Li, Y.; Beeby, S.P.; Craddock, I.J.; Stark, B.H. A Flexible 2.45-GHz Power Harvesting Wristband With Net System Output From −24.3 dBm of RF Power. *IEEE Trans. Microw. Theory Tech.* **2018**, *66*, 380–395. [CrossRef]
68. Paing, T.; Falkenstein, E.; Zane, R.; Popovic, Z. Custom IC for Ultra-low Power RF Energy Harvesting. In Proceedings of the 2009 Twenty-Fourth Annual IEEE Applied Power Electronics Conference and Exposition, Washington, DC, USA, 15–19 February 2009; pp. 1239–1245, ISSN 1048-2334. [CrossRef]
69. Hsieh, P.H.; Chou, C.H.; Chiang, T. An RF Energy Harvester with 44.1% PCE at Input Available Power of -12 dBm. *IEEE Trans. Circuits Syst. I Regul. Pap.* **2015**, *62*, 1528–1537. [CrossRef]
70. Adami, S.E.; Vollaire, C.; Allard, B.; Costa, F.; Haboubi, W.; Cirio, L. Ultra-low Power Autonomous Power Management System with Effective Impedance Matching for RF Energy Harvesting. In Proceedings of the CIPS 2014—8th International Conference on Integrated Power Electronics Systems, Nuremberg, Germany, 25–27 February 2014; pp. 1–6.

71. Wanderoild, Y.; Capitaine, A.; Morel, A.; Pillonnet, G. 100 µW Coreless Flyback Converter for Microbial Fuel Cells Energy Harvesting. In Proceedings of the 2017 New Generation of CAS (NGCAS), Genova, Italy, 6–9 September 2017; pp. 33–36. [CrossRef]
72. Bui, D.H.N. Printed Flexible Antenna for Energy Harvesting. Ph.D. Thesis, Université Grenoble Alpes, Grenoble, France, 2017.
73. Mahfoudi, H.; Takhedmit, H.; Tellache, M.; Boisseau, S. Wireless sensor node remote supply using a compact stacked rectenna array with voltage multipliers at 2.45 GHz. *Int. J. Microw. Wirel. Technol.* **2020**, *12*, 309–315. [CrossRef]
74. Yan, S.; Vandenbosch, G.A.E. Radiation Pattern-Reconfigurable Wearable Antenna Based on Metamaterial Structure. *IEEE Antennas Wirel. Propag. Lett.* **2016**, *15*, 1715–1718. [CrossRef]
75. Kimionis, J.; Isakov, M.; Koh, B.S.; Georgiadis, A.; Tentzeris, M.M. 3D-Printed Origami Packaging With Inkjet-Printed Antennas for RF Harvesting Sensors. *IEEE Trans. Microw. Theory Tech.* **2015**, *63*, 4521–4532. [CrossRef]
76. Ojo, M.O.; Giordano, S.; Procissi, G.; Seitanidis, I.N. A Review of Low-End, Middle-End, and High-End Iot Devices. *IEEE Access* **2018**, *6*, 70528–70554. [CrossRef]
77. Karray, F.; Jmal, M.W.; Garcia-Ortiz, A.; Abid, M.; Obeid, A.M. A Comprehensive Survey on Wireless Sensor Node Hardware Platforms. *Comput. Netw.* **2018**, *144*, 89–110. [CrossRef]
78. Kubaszek, M.; Macheta, J.; Krzak, L.; Worek, C. The analysis of energy consumption in 6TiSCH network nodes working in sub-GHz band. *Int. J. Electron. Telecommun.* **2020**, *66*, 201–210.
79. Zhang, H.; Guo, Y.x.; Zhong, Z.; Wu, W. Cooperative Integration of RF Energy Harvesting and Dedicated WPT for Wireless Sensor Networks. *IEEE Microw. Wirel. Components Lett.* **2019**, *29*, 291–293. [CrossRef]